IEICE TRANSACTIONS

on Communications

VOL. E105-B NO. 12
DECEMBER 2022

A PUBLICATION OF THE COMMUNICATIONS SOCIETY

The Institute of Electronics, Information and Communication Engineers
Kikai-Shinko-Kaikan Bldg., 5-8, Shibakoen 3chome, Minato-ku, TOKYO, 105-0011 JAPAN

IEICE TRANS. COMMUN., VOL.E105–B, NO.12 DECEMBER 2022

PAPER

Accurate Doppler Velocity Estimation by Iterative WKD Algorithm for Pulse-Doppler Radar

Takumi HAYASHI[†], **Takeru ANDO**[†], ***Nonmembers***, ***and*** **Shouhei KIDERA**[†a)], ***Senior Member***

SUMMARY In this study, we propose an accurate range-Doppler analysis algorithm for moving multiple objects in a short range using microwave (including millimeter wave) radars. As a promising Doppler analysis for the above model, we previously proposed a weighted kernel density (WKD) estimator algorithm, which overcomes several disadvantages in coherent integration based methods, such as a trade-off between temporal and frequency resolutions. However, in handling multiple objects like human body, it is difficult to maintain the accuracy of the Doppler velocity estimation, because there are multiple responses from multiple parts of object, like human body, incurring inaccuracies in range or Doppler velocity estimation. To address this issue, we propose an iterative algorithm by exploiting an output of the WKD algorithm. Three-dimensional numerical analysis, assuming a human body model in motion, and experimental tests demonstrate that the proposed algorithm provides more accurate, high-resolution range-Doppler velocity profiles than the original WKD algorithm, without increasing computational complexity. Particularly, the simulation results show that the cumulative probabilities of range errors within 10 mm, and Doppler velocity error within 0.1 m/s are enhanced from 34% (by the former method) to 63% (by the proposed method).

key words: *microwave, millimeter wave radar, Pulse Doppler radar, Doppler velocity estimation, weighted kernel density estimator (WKD), Radar signal processing*

1. Introduction

Microwave radars, including millimeter-wave band, are more robust than optical sensors and work under smog, dense fog, dusty, or other optically challenging conditions. Thus, they are applicable to various object recognition or localization applications, such as human body recognition for collision avoidance required in self-driving scene, or for survivor detection in rescue scene, which should be applicable in the above optically blurred situations. However, short-range radar imaging for multiple complex objects, such as the human body, is still challenging due to a limited aperture size or strong interference caused by numerous responses from an assumed object [1]. Recently, micro-Doppler (MD) analyses for classifying motions of the human body, such as vibrating, rotating, and coning have been intensively investigated for search-and-rescue, security, or surveillance applications [2], [3], using various machine learning based approaches [5]–[7]. The authors of [8] exploited the envelope of a short-time Fourier transform (STFT) spectrogram for arm motion recognition, whereas the authors of [9] focused on MD for road pedestrian detection. The authors of [10] attempted to eliminate micro-motion interference. The method in [11] recognized the total energy expenditure from MD data during walking and running activities.

Several studies have been conducted on Doppler spectrum analysis, including conventional Fourier-transform-based methods, such as the STFT [12]–[14], and the Fourier–Bessel transform [15], and other coherent integration-based methods such as the Wigner–Ville distribution [16], and the pseudo Wigner distribution (SPWD) [17]. However, coherent integration effects, enhancing velocity resolution or noise reduction ability, are not available in handling high range resolution outputs by Capon or compressed sensing (CS) filters because coherent methods require multiple reflection pulses to be recorded within a range-resolution cell along with a coherent processing interval (CPI). Further, an range walk (RW) effect would also degrade an available Doppler velocity resolution due to a limited CPI. Here, the RW effect is defined as a case where a target moves a distance greater than a range resolution of pulse, and a number of pulse hits within the same range resolution cell would be limited, and then, incurring lower velocity resolution. Numerous methods have been employed to address the RW effect, such as the Hough transform [18], [19], Radon-Fourier transform [20]–[22], and keystone transform [23], [24]. Discrete polynomial-phase transform [25] is another promising method for detecting fast-moving objects. However, the above methods assume that the Doppler velocity is invariant over the integration time, which is not applicable in scenarios with longer pulse repetition intervals (PRIs).

As a solution to the aforementioned problem, Setsu et al. proposed a weighted kernel density estimator (WKD)-based time-of-flight (TOF) point, called range-τ point, conversion algorithm [26], in which each range-τ point is converted into its corresponding range-Doppler velocity point. In the WKD algorithm, a Doppler-associated range-τ point is observed for each pulse hit, which means that the temporal resolution is shortened to a PRI. This technique is most advantageous when incorporated with a CS based range extraction filter, where both the super-resolution range and Doppler velocity resolutions are available [26]. This incoherent processing can be implemented on less complex hardware than coherent processing. However, when dealing with data contained by many reflections, the WKD methods' accuracy remains insufficient.

Manuscript received March 7, 2022.
Manuscript revised April 15, 2022.
Manuscript publicized June 29, 2022.

[†]The authors are with Graduate School of Informatics and Engineering, University of Electro-Communications, Chofu-shi, 182-8585 Japan.
a) E-mail: kidera@uec.ac.jp

DOI: 10.1587/transcom.2022EBP3040

To address the aforementioned problem, we newly introduce an iterative data-selection WKD method, which exploits the WKD's unique feature of one-to-one correspondence to a range-Doppler velocity point in each pulse hit. The basis of this method is the data selection in the WKD scheme; specifically, the range-τ point associated with a specific part of the human body, such as the arm, must be processed using only the subset of the range-τ points originating from the same part (arm) of the body. However, unnecessary range-τ points originating from other parts of the body, such as the leg or torso, should be eliminated. The range-τ points can be clustered using the weighting function of the Doppler velocity by using the above property in the proposed algorithm. While the basic concept of this method was reported in [27], it was based on a hard clustering scheme, and only simulation tests were investigated. Furthermore, our iterative data-selection process can eliminate unnecessary data. Note that, the proposed method enables the elimination of unnecessary range-τ points that are associated with inappropriate Doppler velocities, which contribute to further improvements in the Doppler velocity estimations. Because the proposed updating algorithm is simple and avoids hard-clustering schemes as in [27], an unworkable increase in computational complexity can be avoided. Note that, the algorithm proposed in this paper can be applied widely to not only human recognition but also more general Doppler velocity estimation scenarios, where a trade-off between Doppler velocity and temporal resolutions, or unambiguous velocity range would be fatal.

Both geometrical optics approximations and finite-difference time domain (FDTD) based 3-D numerical tests, assuming a 3-D human-body imaging scenario, demonstrate that the proposed algorithm significantly improves the accuracy of Doppler velocity estimations, and provides more informative radar images with an image integration scheme along slow time. In addition, two types of experimental validations using three metallic object with a rotation motion with X-band radar and a real human walking motion with FMCW millimeter wave radar, also show that our proposed method significantly enhances the accuracy of the Doppler velocity by eliminating the redundant responses.

This paper is organized as follows. Section 2 defines the observation model for the short-range scenario, which is assumed for human-body recognition, in which the range-τ points are introduced. Section 3 introduces the original WKD algorithm and the proposed iterative algorithm that uses Doppler-velocity-based data selection. The numerical validations, using both geometrical optics (GO) approximations and the FDTD forward solvers, are presented in Sect. 4. In Sect. 5, two experimental tests, assuming simple metallic spheres and a real human with different walking motions, are presented, which is one of the main updates from [27]. Final part in Sect. 5, we discuss on the qualitative comparison to the existing coherent based Doppler analysis approach, in terms of the PRI, bandwidth, or noise-robustness. The conclusions and other discussions are presented in Sect. 6.

2. Observation Model

Figure 1 shows the observation model. A single set of transmitting and receiving antennas is assumed, with no requirement for directivity. We assume a pulse-Doppler radar system using multiple pulse sequences with a fixed PRI, where a sinusoidal signal is modulated by a pulse function, such as a Gaussian function. The electric field is recorded as $s(t, \tau)$, where t denotes the fast time, and τ denotes the slow-time given by an integer multiple of the PRI as T_{PRI}. Here, $s(t, \tau)$ is redefined as $s(R, \tau)$ with $R = \mathrm{c}t/2$ using the radio-wave speed c. τ denotes the slow-time given by an integer multiple of the PRI. Assuming a number of isolated targets, the recorded signal $s(R, \tau)$ is expressed as:

$$s(R, \tau) = \sum_{k=1}^{N_{\mathrm{T}}} A_k s_{\mathrm{ref}}(R - R_k(\tau)) \tag{1}$$

where A_k denotes a reflection amplitude of k-th target and $s_{\mathrm{ref}}(R)$ denotes a reference signal, usually set to transmittal waveform. $R_k(\tau)$ is determined by the round-trip distance (delay) propagating from the transmitter to the receiver via each target's scattering center point at the slow time τ_i.

To reconstruct the scattering center point or its associated Doppler velocity for each set of range and element location, we introduce the range-τ point as $\boldsymbol{q}_{i,j} \equiv (R_{i,j}, \tau_i)$ at the slow-time $\tau_i = iT_{\mathrm{PRI}}$. Here the subscript i denotes the index number of pulse hit at τ_i, and the subscript j denotes the index number of the extracted range-τ point at each τ_i. These approaches have been widely applied in several studies [26], [28], [30]. To extract the above range point, we first apply the filter, such as a matched filter or the CS filter [26], where the local peak of the filter response would express the distance from the sensor to each target R_k. We now define the output of the filter as $\tilde{s}(R, \tau)$ for each received signal $s(R, \tau)$. Then, the range point is extracted from the local maximum of $|\tilde{s}(R, \tau)|$ along the R direction as:

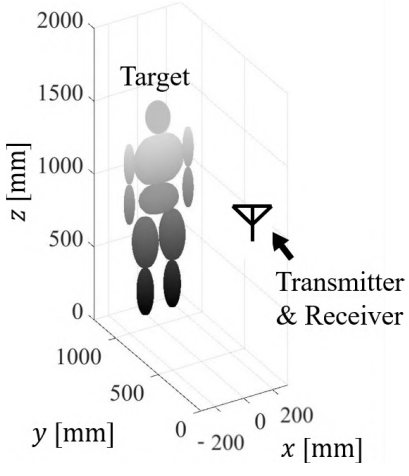

Fig. 1 Observation model.

$$\left.\begin{array}{l} \dfrac{\partial|\tilde{s}(R,\tau)|}{\partial R} = 0 \\ |\tilde{s}(R,\tau)| \geq \alpha \max\limits_{R,\tau} |\tilde{s}(R,\tau)| \end{array}\right\}, \tag{2}$$

where α denotes the threshold parameter.

3. Methods

3.1 Original WKD Algorithm

There are various studies on time-Doppler frequency analysis, but they have not adequately addressed the inherent trade-off between the temporal and frequency (Doppler velocity) resolutions, caused by the coherent integration procedure. In addition, the RW effect worsens under the coherent integration scheme when dealing with large fractional bandwidths, e.g., UWB signals or responses by Capon or CS filters, because each pulse moves beyond the range-resolution cell in PRI.

Setsu et al. proposed a new method to address the above problem [26]. The solution exploits WKD-based range-τ points conversion. This section briefly explains the methodology of the method [26] as follows. This method uses the principle that the inclinations of adjacent range-τ points correspond to the Doppler velocities. The optimal Doppler velocity for $\boldsymbol{q}_{i,j}$ is determined by maximizing the following probabilistic distribution as modeled by weighted Gaussian kernels:

$$\begin{aligned} \hat{v}_d(\boldsymbol{q}_{i,j}) = \arg\max_{v_d} \sum_{k,l} & \exp\left(-\frac{\left||\tilde{s}(\boldsymbol{q}_{i,j})| - |\tilde{s}(\boldsymbol{q}_{k,l})|\right|^2}{2\sigma_s^2}\right) \\ \times \exp\left(-\frac{|\tau_i - \tau_k|^2}{2\sigma_\tau^2}\right) & \exp\left(-\frac{|v_d - \tilde{v}_{\mathrm{d}}(\boldsymbol{q}_{i,j}, \boldsymbol{q}_{k,l})|^2}{2\sigma_{v_d}^2}\right), \end{aligned} \tag{3}$$

where v_{d} is the valuable of the Doppler velocity, $|\tilde{s}(\boldsymbol{q}_{i,j})|$ is the signal strength of the filter output at $\boldsymbol{q}_{i,j}$ and $\tilde{v}_{\mathrm{d}}(\boldsymbol{q}_{i,j}, \boldsymbol{q}_{k,l})$ is defined as $\tilde{v}_{\mathrm{d}}(\boldsymbol{q}_{i,j}, \boldsymbol{q}_{k,l}) \equiv (R_{i,j} - R_{k,l})/(\tau_i - \tau_k)$. σ_s, σ_τ, and σ_{v_d} are empirically determined constants, and their roles are detailed in [26]. These parameters can be determined by considering the assumed PRI or velocity variations. Because σ_τ denotes the correlation length for the slow-time direction, it must be set as a couple of PRIs to deal with the temporal variation of the target. The weighting term $\exp\left(-\frac{\left|v_{\mathrm{d}} - \tilde{v}_{\mathrm{d}}(\boldsymbol{q}_{i,j}, \boldsymbol{q}_{k,l})\right|^2}{2\sigma_{v_{\mathrm{d}}}^2}\right)$ indicates that the Doppler velocity, calculated by the neighboring range-τ points of $\boldsymbol{q}_{i,j}$, should have more weights in Eq. (3). Further, $\sigma_{v_{\mathrm{d}}}$ must be set smaller than the required Doppler velocity resolution. The weighting term $\exp\left(-\frac{\left||\tilde{s}(\boldsymbol{q}_{i,j})| - |\tilde{s}(\boldsymbol{q}_{k,l})|\right|^2}{2\sigma_s^2}\right)$ also indicates that, if the range-τ points belong to the same target, their signal strengths would be similar along the neighbouring PRIs. Further explanations of these parameters or sensitivity studies have been described in [26].

Note that, this method does not require any connecting or tracking procedures for the range-τ points. However, in dealing with many scatterers' object, such as humans, the original WKD would suffer from inaccuracies. This is because Eq. (3) is calculated using all possible combinations of range-τ points included in $\mathcal{Q}_{all}$ for each $\boldsymbol{q}_{i,j}$, where $\mathcal{Q}_{all}$ is defined as a set that contains all measured range-τ points. The above process is totally redundant, and the subset of range-τ points should be adaptively changed according to $\boldsymbol{q}_{i,j}$. For example, the range-τ point associated with a human arm should be assessed using only the subset of range-τ points that originates from the human arm, and not by using range-τ points from the leg or torso. From the above discussion, prior data selection of range-τ points is required to achieve more accurate Doppler velocity estimations.

3.2 Iterative Data Selection Based WKD Algorithm

This section describes the proposed methodology. As described in the previous section, prior data selection of range-τ points is key for accuracy improvement in the WKD method. Thus, we introduce iterative data selection algorithm, namely soft-clustering of range-τ points. To avoid parameter dependency or a complex hard-clustering algorithm issued in [27], the proposed method introduces a new weighting function to Eq. (3). Figure 2 shows the schematic diagram of the proposed method. Here, the weight for each range-τ point is recursively updated using the previous Doppler velocity estimation results. This approach is achieved by the notable feature that the range-τ points and velocity-τ points are solely associated, namely, $\boldsymbol{q}_{i,j}$ and $\hat{v}_d(\boldsymbol{q}_{i,j})$ have a one-to-one correspondence.

As described in the previous subsection, the original WKD algorithm determines $\hat{v}_d(\boldsymbol{q}_{i,j})$ by calculating all possible range-τ points (called SubRPs) for the Doppler velocity at a focused range-τ point $\boldsymbol{q}_{i,j}$ (called MainRP). The correct clustering should occur when the Main RP arises from a specific scatterer (e.g., the right arm), then the subset of SubRPs

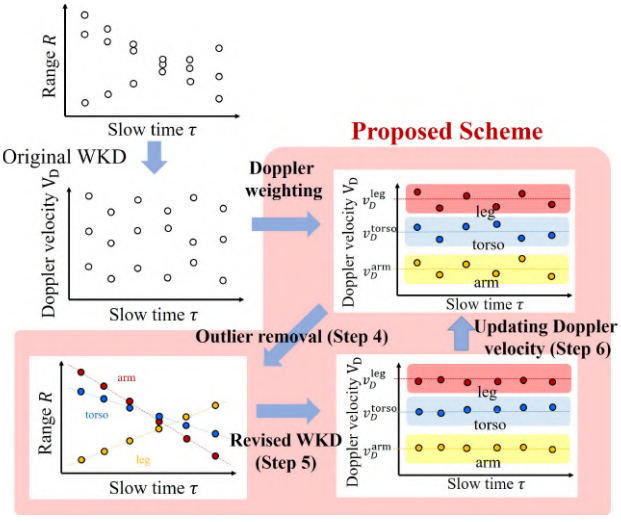

Fig. 2 Schematic procedures of the proposed method, where range-τ points associated with each part of human body is selected and processed in the WKD algorithm, iteratively.

should also be associated with the same scatterer (e.g., right arm). Then, the selection of a range-τ points should be performed, so that the Main RP and SubRps are clustered into the same group. However, this selection scheme should be done without any prior knowledge of each Doppler velocity value. We use an initial estimation of the Doppler velocities as each $\boldsymbol{q}_i$ calculated in Eq. (3).

In the proposed method, the Doppler velocities are then sequentially updated as follows:

$$\hat{v}_{\mathrm{d}}^{(m+1)}(\boldsymbol{q}_{i,j}) = \arg\max_{v_{\mathrm{d}}} \sum_{\boldsymbol{q}_{k,l}\in Q_{i,j}^{(m)}} \exp\left(-\frac{\left||\tilde{s}(\boldsymbol{q}_{i,j})| - |\tilde{s}(\boldsymbol{q}_{k,l})|\right|^2}{2\sigma_s^2}\right) \times \exp\left(-\frac{\left|\tau_i - \tau_k\right|^2}{2\sigma_\tau^2}\right) \exp\left(-\frac{\left|v_{\mathrm{d}}^{(m)}(\boldsymbol{q}_{i,j}) - v_{\mathrm{d}}^{(m)}(\boldsymbol{q}_{k,l})\right|^2}{2\sigma_{v_{\mathrm{c}}}^2}\right) \times \exp\left(-\frac{\left|v_{\mathrm{d}} - \tilde{v}_{\mathrm{d}}(\boldsymbol{q}_{i,j}, \boldsymbol{q}_{k,l})\right|^2}{2\sigma_{v_{\mathrm{d}}}^2}\right), \tag{4}$$

where $\hat{v}_{\mathrm{d}}^{(m)}(\boldsymbol{q}_{i,j})$ denotes the Doppler estimation result of $\boldsymbol{q}_{i,j}$ in the m-th iteration step. $\sigma_{v_{\mathrm{c}}}$ is a constant, which determines the selection criteria in terms of the Doppler velocity. Compared with the original WKD, as in Eq. (3), the Doppler velocity associated $\boldsymbol{q}_{i,j}$ is determined from the selected subset $Q_{i,j}^{(m)}$, not from all possible range-τ points. Here, a subset of range-τ points in the m-th iteration step is defined as $Q_{i,j}^{(m)}$ for each $\boldsymbol{q}_{i,j}$, which is iteratively updated as:

$$Q_{i,j}^{(m)} \equiv \left\{ \boldsymbol{q}_{k,l} \middle| F_{v_{\mathrm{d}}}^{(m-1)}(\boldsymbol{q}_{k,l}) \geq \xi \max_{\boldsymbol{q}_{s,t}} F_{v_{\mathrm{d}}}^{(m-1)}(\boldsymbol{q}_{s,t}) \right\}, \tag{5}$$

where the function $F_{v_{\mathrm{d}}}^{(m-1)}(\boldsymbol{q}_{k,l})$ is defined as the maximum value of the function inside the argmax in Eq. (4) about $\boldsymbol{q}_{k,l}$ at the $m-1$ iteration step. ξ is a zero-dimensional constant threshold determined from statistical characteristics from all $F_{v_{\mathrm{d}}}$ samples, such as Otsu's discrimination analysis [29]. Specifically, the selected subset $Q_{i,j}^{(m)}$ would exclude the range-τ points with lower $F_{v_{\mathrm{d}}}$, which is commonly regarded as an outlier or random noise component. Furthermore, the weight of $\exp\left(-\frac{\left|v_{\mathrm{d}}^{(m)}(\boldsymbol{q}_{i,j}) - v_{\mathrm{d}}^{(m)}(\boldsymbol{q}_{k,l})\right|^2}{2\sigma_{v_{\mathrm{c}}}^2}\right)$ selects the range-τ points $\boldsymbol{q}_{k,l}$ that has a similar Doppler velocity to $v_{\mathrm{d}}^{(m)}(\boldsymbol{q}_{i,j})$, which enhances the Doppler velocity estimation by excluding the unnecessary range-τ points. The above iteration steps are conducted until a preset conversion condition, such as the maximum number of iterations, is satisfied. The above data selection enables the elimination of several unnecessary range-τ points that could be due to random noise or interference effects.

3.3 Procedure of the Proposed Method

The procedure for the proposed method is summarized as follows:

Step 1) Recorded signal is processed by CS filtering [26] for each slow time τ, which is denoted as $s(R, \tau)$.

Step 2) Range-τ points $\boldsymbol{q}_{i,j}$ are extracted from the set of local maxima of $\tilde{s}(R, \tau)$.

Step 3) Initial Doppler velocity $\hat{v}_d^{(1)}(\boldsymbol{q}_{i,j})$ is obtained in Eq. (3).

Step 4) Subset $Q_{i,j}^{(m)}$ is updated in Eq. (5).

Step 5) Doppler velocity is updated as $\hat{v}_{\mathrm{d}}^{(m+1)}(\boldsymbol{q}_{i,j})$ in Eq. (4), using the previously estimated Doppler velocities as $\hat{v}_{\mathrm{d}}^{(m)}(\boldsymbol{q}_{i,j})$.

Step 6) 4) and 5) are recursively repeated until the convergence condition, such as the maximum number of iterations, is satisfied.

Figure 3 gives the flowchart of our proposed method, and the differences from the original WKD scheme detailed in [26] are highlighted. The detail of the CS filter for range-τ points extraction in [26]. Step 4 and 5) represent our innovations from the original WKD scheme. That is, the range-τ points are recursively weighted with the Doppler velocity to attain more accurate Doppler velocity without requiring a computationally expensive radar imaging step like in [26]. In particular, if α is set to a smaller value in Eq. (2), a number of range-τ points, caused by noises, would be extracted. However, the proposed method eliminates these points by iteratively assessing the evaluation function $F_{v_{\mathrm{d}}}$ on the right-hand side of Eq. (4). This is because $F_{v_{\mathrm{d}}}$ less increases in focusing on a randomly distributed range-τ profile (noise), compared with the case on a regularly distributed range-τ profile (signal). In addition, the above proposed iterative updating scheme is not applicable to the coherent integration based methods, this is why we have adopted the WKD algorithm for further improvements of the Doppler velocity estimations.

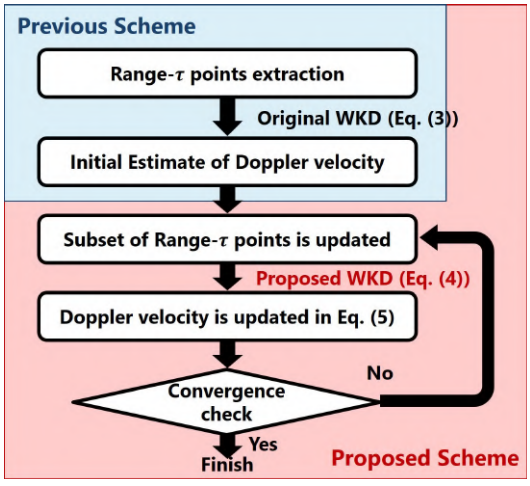

Fig. 3 Flowchart in the proposed method.

4. Results of 3-D Numerical Testing with Human Model

This section describes two 3-D numerical tests that use GO and FDTD analyses. Note that, the GO is a forward solver based on a higher-frequency approximation, with the dominant propagation path determined by optical reflection law [32]. This enables us to assess our method without considering any systematic errors caused by multiple scattering or by the frequency dependency of the scattered signals. Next, the FDTD simulation results would be presented, to assess the accuracy dependency due to multiple reflections or frequency-dependent scattering phenomena from each part of the human body.

4.1 Numerical Settings

This section describes the simulation setup which is common to both GO and FDTD simulation scenarios. A human body target is approximated by an aggregation of 11 ellipsoids (for simplicity), as shown in Fig. 1. While the original and proposed WKD methods are applicable to the single transmitter and receiver models, we assume an array configuration in this numerical model to provide reliable results. The 5×5 planar array with an equal spacing of 50 mm are defined, where 4 transmitters are located at the 4 vertex points of the array, and 25 receivers are placed at 5×5 locations, this configuration means that a combination of 100 data points are processed. Note that, multiple data points obtained using the above array are assumed to be synchronously observed and integrated at each τ. For simplicity, we consider a stepping motion of the human body at the same position as the motion vector along the y axis. Table 1 shows the Doppler velocities for each part of the human body. The transmitted signal is a pulse modulated with a center frequency of 5.0 GHz and bandwidth of 3.0 GHz. The PRI is set to 10.0 ms, and the total number of pulse hits is set to 10; these parameters lead to a total observation time where $T_c = 0.1$ s, and then, $\tau_i = (i-1) \times 10$ ms, for $i = 1, \cdots, 10$. For the Fourier transform-based analysis, the lower limit of the Doppler velocity resolution is 0.30 m/s using the center frequency of 5.0 GHz.

4.2 Results of GO Test

First, we present the results of the GO-based simulation test. Figure 4 shows the results of the two different filters, such as the Wiener and CS filters, where each threshold α is set as 0.5 for the Wiener filter, and 0.3 for the CS filter. The traditional Wiener filter was unable to decompose accurate range points due to a lack of resolution because the GO considers the interference effect among numerous reflection echoes from each part of the human body. However, the CS filter provided a more accurate distribution of range points. The effectiveness of other super-resolution techniques, such as the Capon method, has been demonstrated in [31]. Note

Table 1 Doppler velocity for each part of human body.

Doppler velocity	Parts
−1.0 m/s	Right lower arm & Left lower leg
−0.5 m/s	Right upper arm & Left upper leg
0 m/s	Head & Lower and Upper torso
0.5 m/s	Left upper arm & Right upper leg
1.0 m/s	Left lower arm & Right lower leg

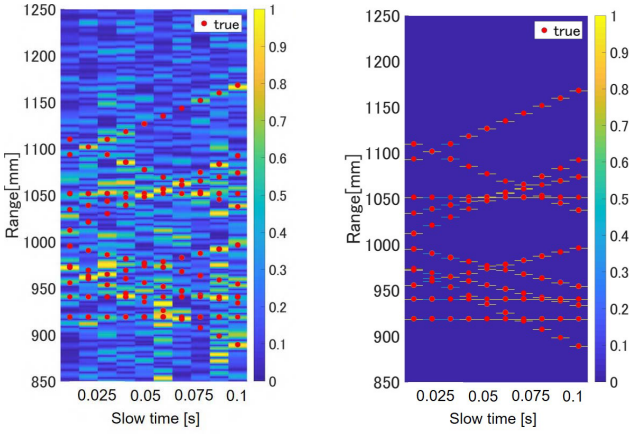

(a) Wiener filter (b) CS filter

Fig. 4 Reflection responses at each slow-time using different filters with the GO generated data. Red dots denote the true profile.

that, the CS filtering requires a large computational time by solving the optimization problem with a large number of unknowns. Furthermore, in dealing with a not-isolated target model, such as a real human body, the sparse assumption is not necessarily valid. These points are the limitation of CS filtering. Figure 5 shows two examples of Doppler velocity estimations using the method described in [26] and the proposed method. Here, the parameters in the original WKD algorithm and in the proposed method are set as, $\sigma_s = 0.7$, $\sigma_{v_d} = 0.05$ m/s, $\sigma_\tau = 50$ ms (5× PRI), and $\xi = 0.2$. The iteration number is 5 and $\sigma_{v_c} = 0.15$ m/s set in the proposed method. It is clear that the proposed method significantly improves the Doppler velocity estimations by iteratively updating the Doppler velocity-based data selections. Note that traditional Fourier transform schemes, such as the STFT or other methods, including Radon Fourier transform, are not effective for application to the CS output because these responses lose carrier frequency and phase information. In addition, especially for the outputs of the CS filter, since the pulse width is quite narrower, there are many RW effects, that pulses are not overlapped along slow time within same range resolution. Instantaneous frequency estimation methods such as Radon–Fourier transform and the Wigner–Ville distribution cannot handle such impulsive CS responses with lost phase and carrier-frequency information. On the contrary, the WKD can handle impulse responses without carrier frequency and phase, because it simply converts the range-τ points (obtained from the response amplitude) to Doppler velocities.

For quantitative validation, we introduced errors in

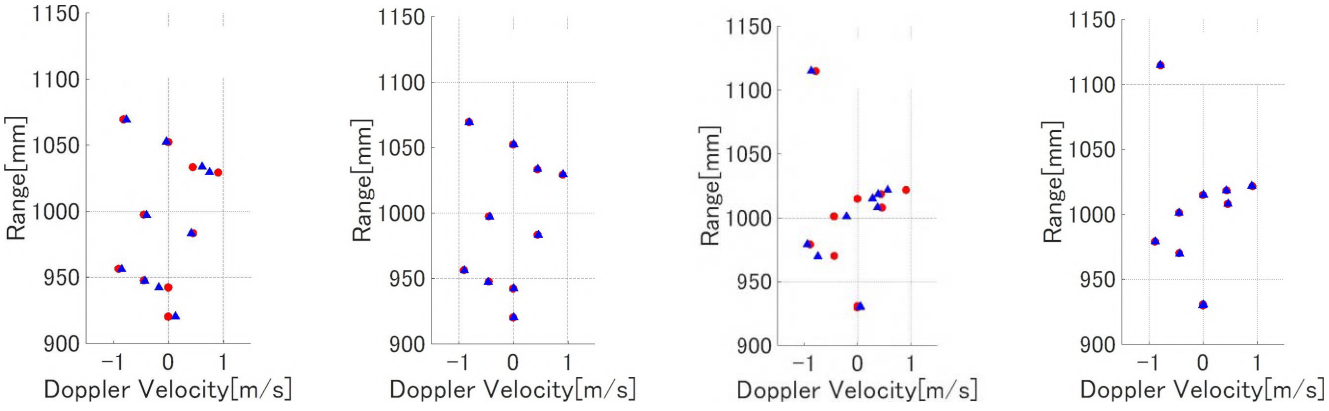

(a) Original WKD (b) Proposed (c) Original WKD (d) Proposed

Fig. 5 Results comparison of Doppler velocity estimation by GO data. (a) and (b): $\boldsymbol{L}^T = (100, 0, 900), \boldsymbol{L}^R = (0, 0, 900)$. (c) and (d): $\boldsymbol{L}^T = (100, 0, 900), \boldsymbol{L}^R = (50, 0, 1100)$. Red solid circles denote true points. Blue solid triangles denote reconstruction points.

Table 2 The cumulative probability of each criteria in the Doppler velocity estimation by GO data.

	Original WKD	Proposed
Number of points	10750	9496
$\lvert\Delta R\rvert \le 10$ mm and $\lvert\Delta v_d\rvert \le 0.1$ m/s	66.3 %	99.3 %
$\lvert\Delta R\rvert \le 20$ mm and $\lvert\Delta v_d\rvert \le 0.1$ m/s	66.7 %	99.3 %
$\lvert\Delta R\rvert \le 20$ mm and $\lvert\Delta v_d\rvert \le 0.2$ m/s	93.9 %	100.0 %

the range as ΔR and the Doppler velocity as Δv_d. Table 2 summarizes the cumulative probability for each error criterion and also further demonstrates the improvements in Doppler velocity estimations produced by the proposed method. These results also indicate that, if we obtain accurate range-τ points, the proposed method retains accurate Doppler velocity profiles, even under conditions with high interference levels. The calculation time was 12 s and 22 s for the original WKD and proposed algorithms with five iterations, respectively, using an Intel Xeon Gold 6130 @2.10 GHz processor with 703 GB of RAM. Notably, because additional computations lasted 10 s more than the original WKD (0 iteration), the average runtime in each iteration step in the proposed algorithm requires only 2 s, which is 6 times faster than the original WKD method because the proposed method processes a smaller number of range-τ points in each cluster in Eq. (5). The estimation accuracies of the original and proposed WKD are dependent on the selected parameters of σ_τ, σ_{v_d} or σ_s. However, a previous study [26] demonstrated that the estimation accuracies of the Doppler velocity are not severely sensitive to these parameters. Further, some studies have optimized these parameters by considering the statistic characteristics of the collected data points, e.g., using the Gaussian mixture model and expectation maximization (EM) algorithm, as in [33].

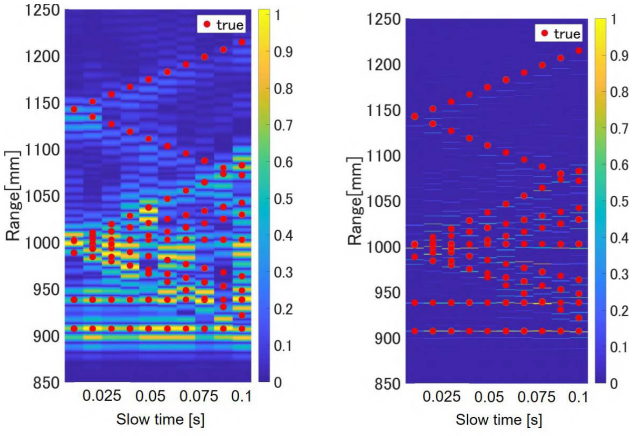

(a) Wiener (b) CS

Fig. 6 Reflection responses at each slow-time using different filters with the FDTD generated data. Red dots denote the true profile.

4.3 Results of FDTD Test

Next, we introduce the results from data generated by the FDTD. In the FDTD model, each part of the human body is assumed to have the same dielectric properties with relative permittivities of 50 and conductivities of 1.0 S/m; these values are derived from the average properties of human tissue. Figure 6 also shows the responses of the range extraction filter and indicates that there are several falsely detected range points, which are due to the multiple scattering effects of the targets, where each threshold α is set as 0.3 for the Wiener filter, and 0.1 for the CS filter. Figure 7 also illustrates two examples of Doppler velocity estimations, where the same parameters of σ_s, σ_{v_d}, σ_τ, σ_{v_c}, and ξ used in the GO simulation test are used. Compared with the results obtained from the GO simulation (an ideal case), there are non-negligible errors in the measured ranges, which are mainly caused by waveform deformations due to the curvatures or volumes of the ellipsoids. Nonetheless, the proposed method provides

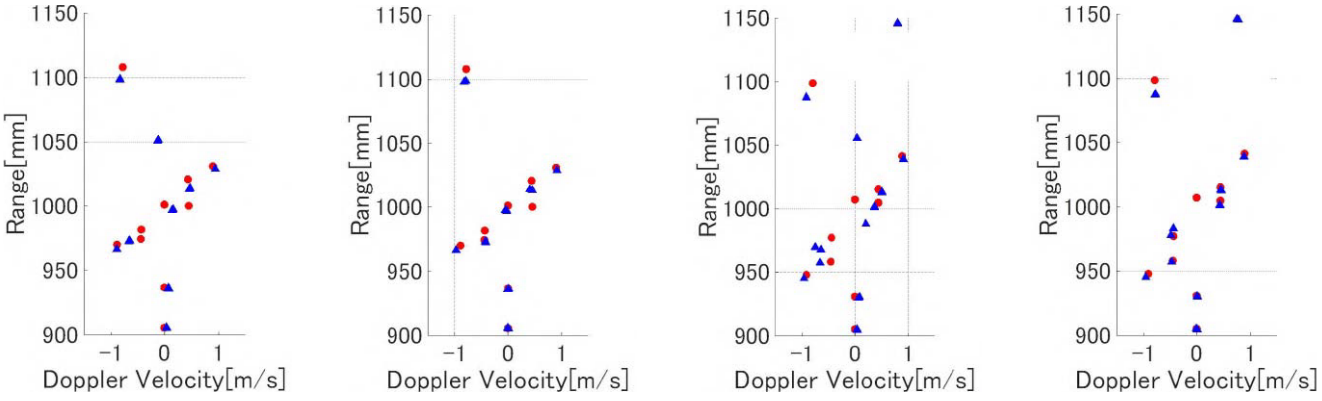

(a) Original WKD (b) Proposed (c) Original WKD (d) Proposed

Fig. 7 Results comparison of Doppler velocity estimation by FDTD data. (a) and (b): $\boldsymbol{L}^T = (100, 0, 900), \boldsymbol{L}^R = (-50, 0, 1100)$. (c) and (d): $\boldsymbol{L}^T = (-100, 0, 1100), \boldsymbol{L}^R = (0, 0, 900)$. Red solid circles denote true points. Blue solid triangles denote reconstruction points.

Table 3 The cumulative probability of each criteria in the Doppler velocity estimation by FDTD data in noiseless case.

	Original WKD	Proposed
Number of points	17336	10411
$\lvert\Delta R\rvert \le 10$ mm and $\lvert\Delta v_d\rvert \le 0.1$ m/s	34.4%	63.1%
$\lvert\Delta R\rvert \le 20$ mm and $\lvert\Delta v_d\rvert \le 0.1$ m/s	42.8%	77.2%
$\lvert\Delta R\rvert \le 20$ mm and $\lvert\Delta v_d\rvert \le 0.2$ m/s	60.3%	81.8%

much better performance for Doppler velocity estimations in this scenario. It also eliminates unnecessary Doppler velocities, which might be due to multiple scattering effects. Table 3 quantitatively demonstrates the errors. Note that the ideal case would consist of obtaining 11,000 points for the Doppler velocity points because we assumed 11 isolated, ellipsoidal targets and a combination of 4 transmitters and 25 receivers. Thus, the initial number of Doppler velocity points (17,336) is too large and also includes unnecessary points due to multiple scattering effects, which have been removed through the iterative assessment in the proposed method using Eq. (5). In addition, as shown in Table 3, the proposed method notably enhances the accuracies of the estimated Doppler velocity points compared with that provided by the original WKD method, even in the FDTD scenario. This is because our algorithm reduces the weight of the unnecessary SubRPs in Eq. (4), and thus improves the accuracy of the Doppler velocities. We should note that the calculation times are 31 s for the original WKD and 55 s for the proposed method with 5 iteration steps, using the Intel Xeon Gold 6130 @2.10 GHz processor with 703 GB of RAM. These increases from the GO simulation are due to a larger number of range-τ points, and the average runtime during each iteration step in the proposed method requires only 4.8 s, which is 6.5 times faster than that by the original WKD method.

A sensitivity to an additive random noise is investigated as follows. Gaussian white noise is added to the received

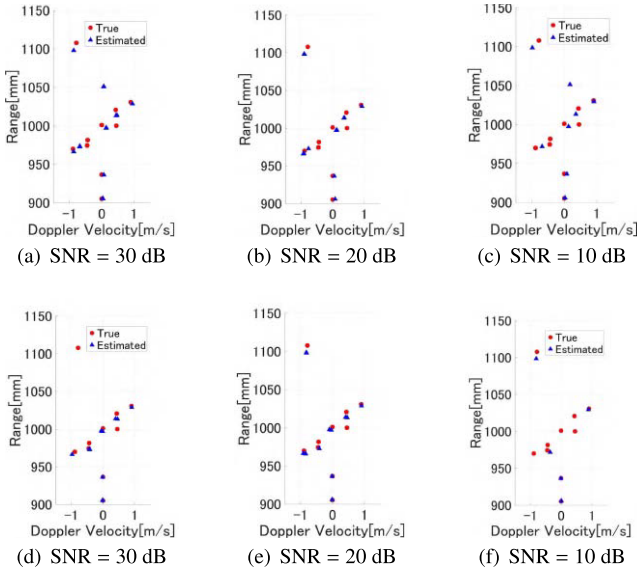

(a) SNR = 30 dB (b) SNR = 20 dB (c) SNR = 10 dB

(d) SNR = 30 dB (e) SNR = 20 dB (f) SNR = 10 dB

Fig. 8 Results comparison of Doppler velocity estimation by FDTD data in each SNR level at the observation pattern as $\boldsymbol{L}^T = (100, 0, 900), \boldsymbol{L}^R = (-50, 0, 1100)$. (a)–(c): Original WKD method. (d)–(f): Proposed method. Red solid circles denote true points. Blue solid triangles denote reconstruction points.

signal. The signal to noise ratio (SNR) is defined as the ratio of the maximum power of the received signals to the average power of the noise in the time domain. We tested three SNR cases, namely 10 dB, 20 dB, and 30 dB. Here, each method or SNR level assumes the same pattern of Gaussian random data. Figure 8 shows the comparisons between the method described in [26] and the proposed method for each SNR level. These figures demonstrate that our proposed method retains its superiority to the method described in [26] for any SNR case, and it is considered that the proposed method eliminates the falsely detected range points in the iterative procedure. This is because the WKD method assesses not only the neighbouring range-τ points to determine the Doppler velocity in Eq. (3) or (4), but also all pos-

Table 4 The cumulative probability of each criteria in the Doppler velocity estimation by the proposed method using the FDTD data at different SNR levels.

	SNR=30 dB	SNR=20 dB	SNR=10 dB
Number of total points	8017	7834	6217
$\|\Delta R\| \le 10$ mm and $\|\Delta v_d\| \le 0.1$ m/s	73.6 %	73.8 %	71.0 %
$\|\Delta R\| \le 20$ mm and $\|\Delta v_d\| \le 0.1$ m/s	85.0 %	85.6 %	84.5 %
$\|\Delta R\| \le 20$ mm and $\|\Delta v_d\| \le 0.2$ m/s	89.0 %	89.4 %	89.4 %

sible combinations of range-τ points, which could provide considerable noise-robustness by an averaging effect. Furthermore, Table 4 compares the total number of estimated points and cumulative probability, satisfying each error criteria as to range and velocity estimation provided by the proposed method for three SNR cases. The table shows that the number of correct estimation points decreases at low SNR, which is also illustrated in Fig. 8. However, the ratio satisfying the specific error criteria such as $\Delta R \le 10$ mm or $\Delta v_d \le 0.1$ m/s, namely, the cumulative probability is maintained even at low SNR values. It then, demonstrates our method maintains the accuracy even under lower SNR case and using incoherent processing. Note that, the cumulative probability at SNR = 20 dB is slightly better than that obtained at SNR =30 dB, which may be caused by the randomness of noise. However, the total available range-τ points considerably decrease at lower SNRs when compared with the original number of range-τ points, 11000. Note that, these results are provided by a specific random pattern, and statistical analysis should be used to reach a convincing conclusion.

5. Experimental Validation

In the experimental test, we introduce two scenarios. The first is an X-band radar measurement with three spherical targets, which enables us to quantitatively validate each method. The other is with millimeter-wave radar equipment in the 24 GHz band, where a real human body in walking motion is assumed, to demonstrate our proposed method in a realistic situation.

5.1 Target: Metallic Spheres

5.1.1 Settings

First, we performed an experimental validation using X-band UWB radar equipment. The geometrical setup of the experiment is shown in Fig. 9, and uses a UWB impulse radar system from Sakura Tech Corp. This system uses a center frequency of 8.5 GHz and has a bandwidth of 1.5 GHz, which is defined as the frequency band bounded by points 10 dB below the peak power [35]. Thus, the range resolution is calculated as 100 mm. The two Fermi antennas are vertically stacked and the upper and lower antennas with

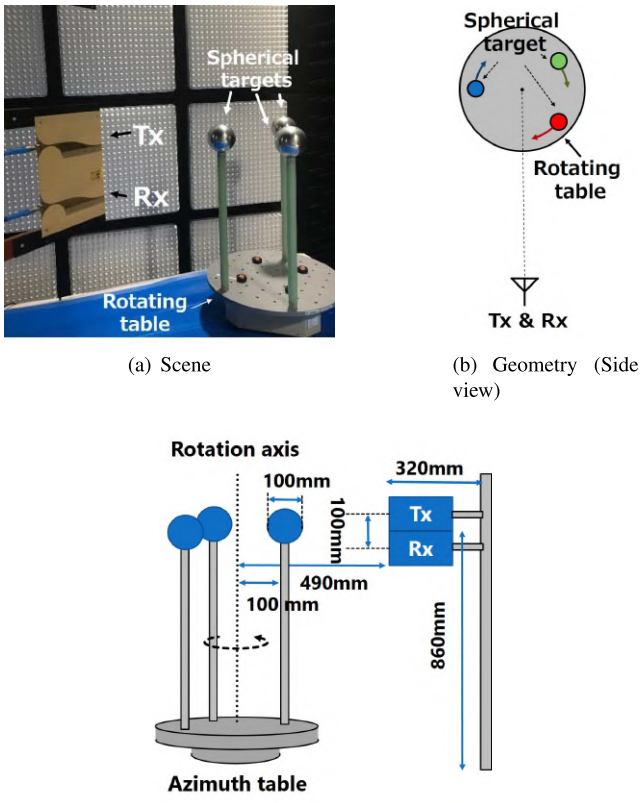

(a) Scene

(b) Geometry (Side view)

(c) Geometry (Top view)

Fig. 9 Experimental setup.

100-mm spacing are the transmitter and receiver, respectively. The 3-dB beam widths of the antenna are 40° along the E- and H-planes. Three metallic spheres with a 100-mm diameter are rotated by the azimuth angle controller over a range of π in the clockwise direction with a spacing of $\pi/36$ radian, and 36 observations are then conducted. To obtain accurate Doppler and range profiles for the target, stop-and-go observations are carried out for each rotation angle (pulse hit). The distance from the observation point to the rotation axis of the table is 490 mm. Here, the PRI is set to 156.25 ms and the total observation time is 5.625 s with 36 pulse hits.

5.1.2 Results and Discussions

Figure 10 shows the STFT results for which the rectangular temporal window was set to 1.875 s. This means that, for this case, the Doppler velocity resolution is 0.009 m/s and the unambiguous Doppler velocity is ±0.197 m/s. As in Fig. 10, the STFT analysis could not provide accurate Doppler velocity responses and provide lower resolution of the Doppler velocities caused by the time-variant Doppler velocities in the CPI, which is inherent problem in the Fourier transform based method, like Radon-Fourier or other coherent based approaches. Also, the actual Doppler velocities range to above 1.0 m/s, which are clearly greater than the upper limit of the unambiguous velocity of 0.0575 m/s. It should be also noted that the coherent inte-

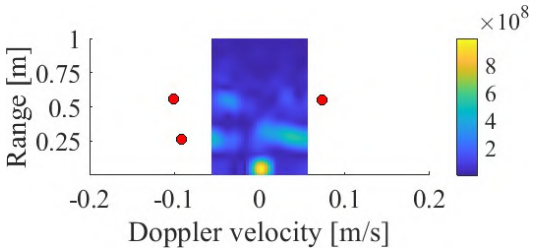

(a) $0\text{s} \le \tau \le 1.875\text{s}$

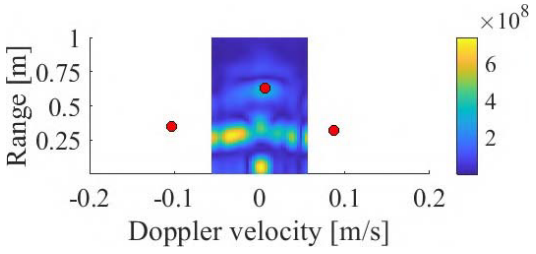

(b) $1.875\text{s} \le \tau \le 3.75\text{s}$

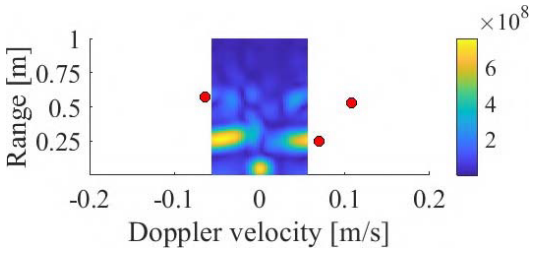

(c) $3.75\text{s} \le \tau \le 5.625\text{s}$

Fig. 10 STFT responses in range-Doppler velocity space using the temporal window width of 1.875 sec. Red solid circles denote the actual Doppler velocity at the center of each time window. Color bar denotes the strength of STFT responses.

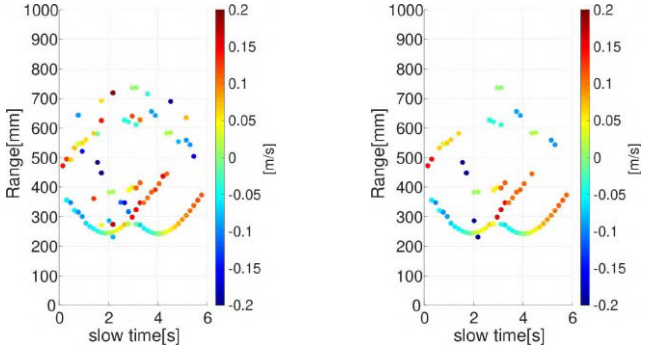

(a) Original WKD (b) Proposed

Fig. 11 Outputs of CS filters and the Doppler velocity estimations by each method, where the color denotes the Doppler velocity estimated at each range-τ point.

gration schemes, such as STFT or Wigner-distribution analyses, require a sufficient CPI for obtaining the necessary velocity resolution and coherent averaging effect to boost the SNR.

In contrast, Fig. 11 shows the responses obtained by the CS filter for each slow time, as well as the range-τ extractions, and the color of each point denotes the estimated

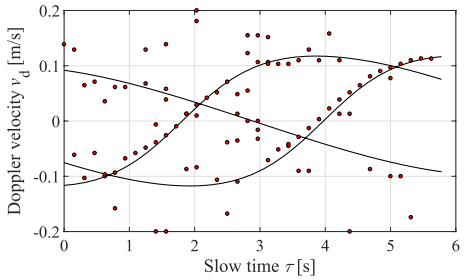

(a) Method[26]

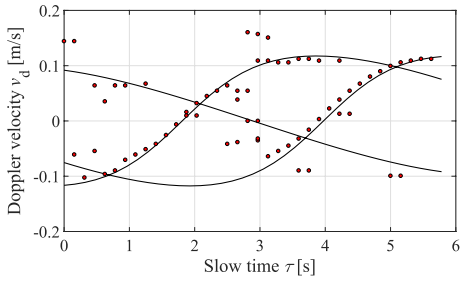

(b) Proposed

Fig. 12 (a) and (b): Doppler velocity estimation results at each slow-time with the experiment data. Black curves denote the actual Doppler velocity curves.

Doppler velocity. Figure 12 also compares the results of the Doppler velocity estimation in Doppler-τ space. The following parameters were set in the WKD algorithm, $\alpha = 0.2$, $\sigma_s = 0.7$, $\sigma_{v_d} = 0.02$ m/s, and $\sigma_\tau = 312.5$ ms (2× PRI). The iteration number is 10 and $\sigma_{v_c} = 0.2$ m/s and $\xi = 0.2$ set in the proposed method. Figure 11 demonstrates that while the front two target responses are clearly observed, some responses from the back targets are lost because of shadowing effects. Figure 12 shows the slow-time and Doppler profile, and shows that our proposed method provides more accurate Doppler profiles by eliminating the redundant outliers that were present in the original WKD method. Table 5 summarizes the cumulative probability of each error criterion; this result also demonstrates that our proposed algorithm successfully improves the accuracy of the Doppler velocity estimations. Note that when comparing the results obtained in the simulation described in Sect. 4, the accuracy improvement from the original WKD method is not remarkable. This is because, since the experimental setup assumes that the three spheres have a certain separation, and this situation would not cause the outliers so much and the original WKD retains its accuracy at a certain level. Then, the superiority of our proposed method would be more clear in assuming a greater number of target cases, as in the simulation model, because the iterative clustering scheme better decomposes the range-τ response from each target.

5.2 Target: Real Human

5.2.1 Setting

Next, we investigate a real human body target in a walking

Table 5 The cumulative probability of each criteria in the Doppler velocity estimation by the experimental data.

	Original WKD	Proposed
Number of points	93	70
$\|\Delta R\| \le 10$ mm and $\|\Delta v_d\| \le 0.01$ m/s	41.1% (38/93)	50.0% (35/70)
$\|\Delta R\| \le 20$ mm and $\|\Delta v_d\| \le 0.02$ m/s	50.6% (47/93)	55.7% (39/70)
$\|\Delta R\| \le 20$ mm and $\|\Delta v_d\| \le 0.01$ m/s	42.2% (40/93)	52.9% (37/70)

(a) Radar and Target (b) Walking scene

Fig. 13 Experimental setup. (a): Arrangement for MMW radar and human body target. (b): Walking scene with slow and normal speed.

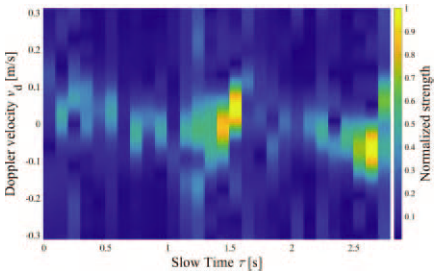

(a) Case 1

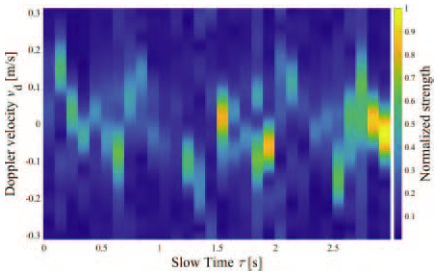

(b) Case 2

Fig. 14 Doppler velocity responses as a function of slow time τ obtaibed by the STFT based analysis with the temporal window width of 0.1 sec.

motion, using FMCW millimeter wave radar with a center frequency of 24 GHz and 2.0 GHz bandwidth (Sakura Tech Corp). Because we could not apply the stop-and-go observation in the real human walking scenario, we used the above FMCW radar, where accurate PRI data acquisition is possible. Figure 13 illustrates the experimental setup, including the radar and the human target. Both the E- and H-plane of the patch antenna are 15 degrees in the 3-dB criteria. The PRI is 10 ms, and denotes an unambiguous velocity as ±0.31 m/s, that is much less than the maximum velocity of the arm or leg in the walking motion with the order of ±1.0 m/s. During the test, the human subject takes a stepping motion on a certain spot, which is approximately 1500 mm far from the radar site. Here, the two walking motion cases are investigated, Case 1 (called slow speed) is the case of the walking motion with an average interval of 3.2 s, and Case 2 (called normal speed) is that with an average interval of 1.4 s.

5.2.2 Results and Discussions

Figure 14 shows the Doppler slow-time profile given by the STFT results. The CPI is set to 0.10 s and $R = 1500$ mm. In this case, the Doppler velocity resolution is 0.062 m/s. As shown in this figure, the STFT responses characterize the Doppler velocity variance to some extent, but the available unambiguous velocity (±0.31 m/s) does not cover the maximum Doppler velocity of an arm or leg, which exceeds ±1.5 m/s at normal speeds. The STFT is useless in such large PRI cases. Figure 15 shows the measured range-τ profiles and the extracted range-τ points with the matched filter is applied, where the reference profiles are also compared. Note that, to generate a reliable reference profile of range-τ points, all the range-τ points of 64 channels (4 transmitters × 16 receivers) are assessed, which are available by this radar system, simultaneously (denoting red points in (a) and (d) in Fig. 15). Because the spacing between the 3-D arrays (6.2 mm) is much smaller than the distance from the array to the target, profiles of all channels would express the same profiles. Furthermore, in Fig. 16(a) and (d), we introduce the outlier detection algorithm of these range-τ points to select a reliable range-τ profile. Here, we introduced the angle-based outlier detection (ABOD) algorithm [36] to assess the outlier at the measured range-τ points. We then consider the remaining range-τ points (blue dots in Fig. 16(a) and (d)) as a reference profile. By using these results, Table 6 shows the cumulative probabilities for including the outliers in the original and proposed WKD methods by changing the thresholds of the ABOD. These results quantitatively verify that the iterative clustering approach in our proposed method significantly reduces the ratio of outlier inclusion.

Furthermore, Fig. 16 shows the Doppler-τ profiles associated solely with range-τ points, with the data shown in Fig. 15 by each method. Here, $\alpha = 0.3$, $\xi = 0.2$, $\sigma_s = 10^6$, $\sigma_\tau = 0.05$ s, and $\sigma_{v_d} = 0.4$ m/s, $\sigma_{v_c} = 0.15$ m/s are set. Note that, a quantitative error for the Doppler velocity is hardly assessed in this case, because we could not obtain a statistically convincing reference (ground truth) profiles. However, the outlier detection results in range-τ points in Table 6 guaranteed that our proposed method effectively removes the unnecessary estimated points even in real human walking case.

The computational run times for the original WKD and the proposed method are 13 s and 15 s, respectively, with the proposed method using only two iterations of data clustering. Note that the proposed method requires only 2 s of additional processing time for a significant improvement in

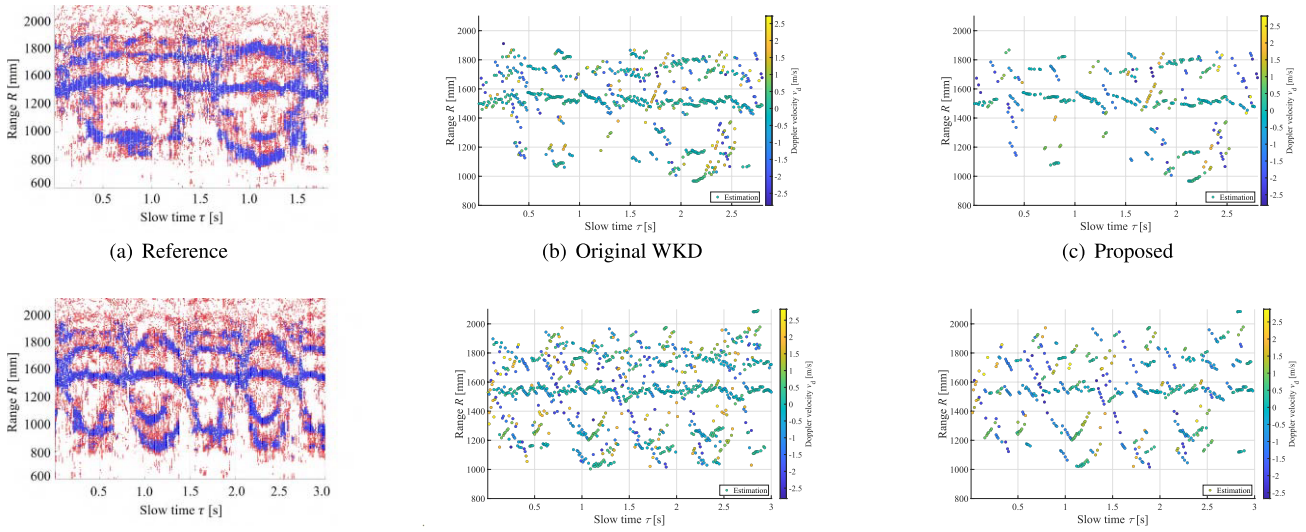

(a) Reference (b) Original WKD (c) Proposed

(d) Reference (e) Original WKD (f) Proposed

Fig. 15 Range-τ responses using the matched filter assuming real human walking motion in the experiment, where the color denotes the Doppler velocities estimated by the original WKD and the proposed WKD algorithms. The blue and red dots in reference profile (a) and (d) denote all the range-τ points at 64 channels with and without applying the ABOD outlier elimination, where the threshold is set to 5%. (a), (b), and (c): Case 1 (Slow speed). (d), (e), and (f): Case 2 (Normal speed).

Table 6 Cumulative probabilities of including the outlier points in each human walking case in the experiment, in changing the threshold in the ABOD detection.

	Case 1		Case 2	
Threshold	Original WKD	Proposed	Original WKD	Proposed
5%	16.3%	14.8%	18.0%	15.0%
10%	24.3%	22.0%	26.7%	22.4%
20%	35.6%	32.5%	38.1%	33.0%

accuracy. This is possible because the WKD algorithm is applied to each cluster of range-τ points as $Q_{i,j}^{(m)}$ in Eq. (4). Nonetheless, the total processing time is required 15 seconds because we deal with the range-τ points over 2 sec period. This should be largely reduced in assuming the practical scenario, like collision avoidance, using a smaller set of slow-time data.

5.3 Qualitative Comparison to Coherent Approach

This section describes the applicability or limitation of the WKD based method, compared with the traditional coherent integration based method.

5.3.1 PRI

First, we show the required PRI and available Doppler velocity resolutions in the coherent integration based method assuming human walking motion and using the Fourier transform based method. For example, if require a temporal resolution of 10 ms and an unambiguous velocity range of ±3 m/s assuming the human walking motion scenario, the PRI and the available Doppler velocity resolutions are summarized 5.8 GHz, 24 GHz, and 61 GHz as in Table 7 at the typical industry science and medical (ISM) band frequency. As shown in Table 7, while the PRI would be achievable in the typical radar equipment in the case of 5.8 GHz and 24 GHz band, the Doppler velocity resolution is insufficient to follow the detailed motion of each part of the human body. Additionally, at 61 GHz, it offers 0.25 m/s velocity resolution, and is possibly applicable to tracking the human walking motion with micro-Doppler analysis, even in using the STFT analysis. However, in the lower PRF, the WKD method would have an advantage in terms of temporal and velocity resolution without the limitation of unambiguous velocity range.

5.3.2 Bandwidth (BW)

Although this study was conducted with a low PRF, the original and proposed WKD applies to higher-PRF scenarios with a wide bandwidth (BW), such as those used in the ISM band automobile radar. In the case of the higher-PRF radar, the WKD algorithm can provide a higher temporal resolution, because more densely sampled range-τ points along the slow-time direction can be processed. Furthermore, if σ_τ, as the correlation length for τ, becomes large, the velocity estimation accuracy will be enhanced by the averaging effect. For a wider BW, the RW effect is predicted to be more severe because the neighboring pulses do not overlap within

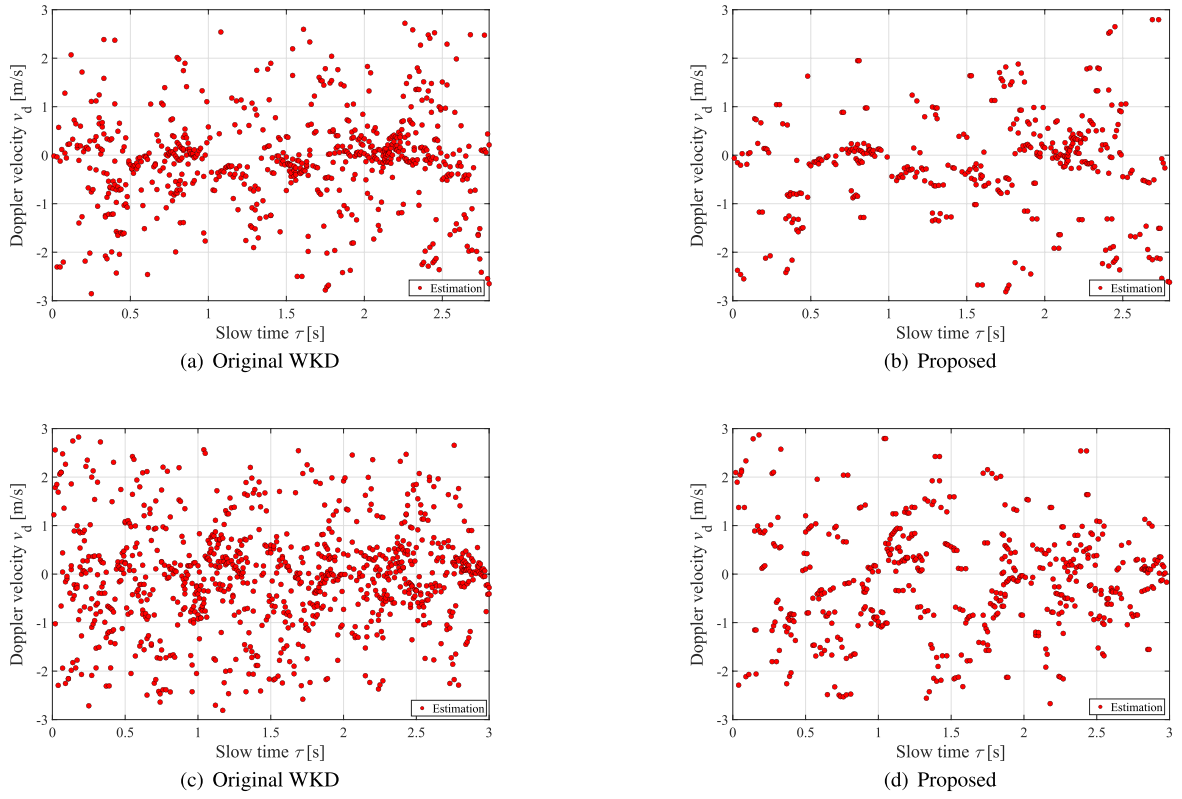

(a) Original WKD (b) Proposed

(c) Original WKD (d) Proposed

Fig. 16 Doppler-τ responses using the matched filter assuming real human walking motion in the experiment. (a) and (b): Case 1 (Slow speed). (c) and (d): Case 2 (Normal speed).

Table 7 Available Doppler velocity resolution with STFT analysis and PRI in each ISM band.

Frequency	5.8 GHz	24 GHz	61 GHz
PRI	4 ms	1040 μs,	41 μs
Doppler velocity resolution	2.58 m/s	0.62 m/s	0.25 m/s

a higher range-resolution cell. Therefore, the WKD algorithm has a significant advantage in properly addressing the aforementioned RW problem. In addition, super-resolution techniques, such as CS filters, should decompose the target responses along the range direction in the case of a narrower BW, such as the 24-GHz ISM band. Thus, when using such super-resolution techniques, as those demonstrated in Sects. 4.2 or 4.3, the RW effect would be severe.

5.3.3 Noise Robustness

Finally, our proposed method has some shortcomings or limitations compared to coherent-integration-based methods, such as STFT or Wigner distribution analysis. For example, when a chirp is processed based on Wigner distribution analysis, the SNR increases N-fold, where N is the number of pulses in the CPI. The WKD method does not have this advantage. However, these coherent integration schemes assume that the Doppler velocity is invariant within the CPI. This assumption would be violated in a longer-PRI scenario and when dealing with human walking motions or a rotating target, as assumed in our experiments. Coherence-based methods offer higher-resolution Doppler velocity profiles with a narrower signal bandwidth, or can be a higher S/N gain. We expect that the data decomposition based on wave number like [37], can address these limitations, assuming that the higher-frequency MMW radar with much narrower bandwidth case and higher coherent gain or range resolution would be available for range-τ point extraction. The aforementioned incorporation is also within our future scope.

6. Conclusion

This paper introduces a new algorithm for iterative data selection (soft clustering) using the WKD-based Doppler velocity estimator. The proposed method exploits a unique feature of the WKD algorithm; each range-τ point has a one-to-one correspondence with a range-Doppler velocity point. In this method, the outliers generated by interference between targets or random noises are effectively eliminated using iterative thresholding algorithm with the WKD's evaluation function. Using the iterative data weighting method, the 3-D GO and FDTD numerical tests, assuming a human-body imaging scenario, have quantitatively demonstrated that our proposed method significantly improves the Doppler velocity estimation accuracies. Specifically, in the FDTD-based numerical test, the proposed algorithm retains over 80% cumulative probability in satisfying the range and velocity errors within 20 mm and 0.2 m/s, re-

spectively, which is 20% greater than that obtained by the original WKD, and it requires 55 s to handle all range-τ points. In addition, the two types of experimental validations are investigated. The first is with the X-band radar assuming three rotating metallic spheres and the other using the FMCW millimeter wave radar for real human walking targets of different speeds. These results demonstrated that the proposed algorithm improved the accuracy of the Doppler velocity estimation with only a 15% increase in the computation time compared with the original WKD algorithm.

Note that our method is naturally extendible to other moving objects and not limited to human walking analysis. In this study, we focused on a human-body classification, but the micro-Doppler effects of other targets, such as animals, cyclists, and other fluctuating objects, should also be classified. In future work, we will tackle this task by exploiting the higher resolution and accuracy features of Doppler velocity estimation in the proposed method.

References

[1] S. Gui, J. Li, F. Zuo, and Y. Pi, "Analysis of security imaging method for walking human screening with single channel synthetic aperture radar," IEEE Access, vol.7, pp.111363–111374, July 2019.
[2] C. Ding, H. Hong, Y. Zou, H. Chu, X. Zhu, F. Fioranelli, J. Le Kernec, and C. Li, "Continuous human motion recognition with a dynamic range-Doppler trajectory method based on FMCW radar," IEEE Trans. Geosci. Remote Sens., vol.57, no.9, pp.6821–6831, Sept. 2019.
[3] Y. Ding, Y. Sun, G. Huang, R. Liu, X. Yu, and X. Xu, "Human target localization using Doppler through-wall radar based on micro-Doppler frequency estimation," IEEE Sensors J., vol.20, no.15, pp.8778–8788, Aug. 2020.
[4] J. Zhu, H. Chen, and W. Ye, "A hybrid CNN–LSTM network for the classification of human activities based on micro-Doppler radar," IEEE Access, vol.8, pp.24713–24720, Feb. 2020.
[5] Y. Kim and H. Ling, "Human activity classification based on micro-Doppler signatures using a support vector machine," IEEE Trans. Geosci. Remote Sens., vol.47, pp.1328–1337, May 2009.
[6] X. Huang, J. Ding, D. Liang, and L. Wen, "Multi-person recognition using separated micro-Doppler signatures," IEEE Sensors J., vol.20, no.12, pp.6605–6611, June 2020.
[7] R. Du, Y. Fan, and J. Wang, "Pedestrian and bicyclist identification through micro Doppler signature with different approaching aspect angles," IEEE Sensors J., vol.18, no.9, pp.3827–3835, May 2018.
[8] Z. Zeng, M.G. Amin, and, T. Shan, "Automatic arm motion recognition based on radar micro-Doppler signature envelopes," IEEE Sensors J., vol.20, no.22, pp.13523–13532, Nov. 2020.
[9] A. Lazaro, M. Lazaro, R. Villarino, and P. De Paco, "New radar micro-Doppler tag for road safety based on the signature of rotating backscatters," IEEE Sensors J., vol.21, no.6, pp.8604–8612, March 2021.
[10] R. Zhao, X. Ma, X. Liu, and F. Li, "Continuous human motion recognition using micro-Doppler signatures in the scenario with micro motion interference," IEEE Sensors J., vol.21, no.4, pp.5022–5034, Feb. 2021.
[11] Y. Kim, S. Choudhury, and H. Kong, "Application of micro-Doppler signatures for estimation of total energy expenditure in humans for walking/running activities," IEEE Access, vol.4, pp.1560–1569, March 2016.
[12] M. Gustafsson, A. Andersson, T. Johansson, S. Nilsson, A. Sume, and A. Örbom, "Extraction of human micro-Doppler signature in an urban environment using a "sensing-behind-the-corner" radar," IEEE Geosci. Remote Sens. Lett., vol.13, no.2, pp.187–191, Feb. 2016.
[13] L. Du, L. Li, B. Wang, and J. Xiao, "Micro-Doppler feature extraction based on time-frequency spectrogram for ground moving targets classification with low-resolution radar," IEEE Sensors J., vol.16, no.10, pp.3756–3763, May 2016.
[14] X. Qiao, T. Shan, R. Tao, X. Bai, and J. Zhao, "Separation of human micro-Doppler signals based on short-time fractional Fourier transform," IEEE Sensors J., vol.19, no.24, pp.12205–12216, Dec. 2019.
[15] P. Suresh, T. Thayaparan, T. Obulesu, and K. Venkataramaniah, "Extracting micro-Doppler radar signatures from rotating targets using Fourier-Bessel transform and time-frequency analysis," IEEE Trans. Geosci. Remote Sens., vol.52, no.6, pp.3204–3210, June 2013.
[16] B. Boashash and P.O. Shea, "Polynomial Wigner-Ville distributions and their relationship to time-varying higher order spectra," IEEE Trans. Signal Process., vol.42, no.1, pp.216–220, Jan. 1994.
[17] F. Hlawatsch and G.F. Boudreaux-Bartels, "Linear quadratic time-frequency signal representations," IEEE Signal Process. Mag., vol.9, no.2, pp.21–67, April 1992.
[18] B.D. Carlson, E.D. Evans, and S.L. Wilson, "Search radar detection and track with the Hough transform. I. system concept," IEEE Trans. Aerosp. Electron. Syst., vol.30, no.1, pp.102–108, Jan. 1994.
[19] Y. Zhou, D. Bi, A. Shen, and X. Wang, "Hough transform-based large micro-motion target detection and estimation in synthetic aperture radar," IET Radar, Sonar & Navigation, vol.13, no.4, pp.558–565, April 2019.
[20] J. Xu, J. Yu, Y.N. Peng, and X.G. Xia, "Radon-Fourier transform (RFT) for radar target detection, I: generalized Doppler filter bank processing," IEEE Trans. Aerosp. Electron. Syst., vol.47, no.2, pp.1186–1202, April 2011.
[21] W. Wang, C. Chen, G. Qu, Y. Zuo, and G. Zeng, "Low-observable target detection using two-stage RFRFT," IET Radar, Sonar & Navigation, vol.13, no.4, pp.653–663, April 2019.
[22] H. Wang, W. Huang, and Y. Jiang, "Moving target integration by exponentially weighted recursive RFT," IET Radar, Sonar & Navigation, vol.13, no.11, pp.2008–2014, Nov. 2019.
[23] P.H. Huang, G.S. Liao, Z.W. Yang, and X.G. Xia, "Long-time coherent integration for weak maneuvering target detection and high-order motion parameter estimation based on keystone trasform," IEEE Trans. Signal Process., vol.64, no.15, pp.4013–4026, Aug. 2016.
[24] Z. Sun, X.L. Li, W. Yi, G.L. Cui, and L.J. Kong, "Detection of weak maneuvering target based on keystone transform and matched filtering process," Signal Processing, vol.140, pp.127–138, May 2017.
[25] C. Pang, S. Liu, and Y. Han, "Coherent detection algorithm for radar maneuvering targets based on discrete polynomial-phase transform," IEEE Sel. Topics Appl. Earth Observ., vol.12, no.9, pp.3412–3422, Sept. 2019.
[26] M. Setsu, T. Hayashi, J. He, and S. Kidera, "Super-resolution Doppler velocity estimation by kernel based range-τ point conversions for UWB short range radars," IEEE Trans. Geosci. Remote Sens., vol.58, no.4, pp.2430–2443, April 2020.
[27] T. Hayashi and S. Kidera, "Iterative data clustering algorithm of Doppler-associated RPM imaging for UWB human body imaging radar" Proc. 2019 Photonics & Electromagnetics Research Symposium (PIERS 2019), June 2019.
[28] T. Sakamoto, T. Sato, P. Aubry, and A. Yarovoy, "Fast imaging method for security systems using ultrawideband radar," IEEE Trans. Aerosp. Electron. Syst., vol.52, no.2, pp.658–670, April 2016.
[29] N. Otsu, "A threshold selection method from gray-level histograms," IEEE Trans. Syst., Man, Cybern., vol.9, no.1, pp.62–66, Jan. 1979.
[30] S. Kidera, T. Sakamoto, and T. Sato, "Accurate UWB radar three-dimensional imaging algorithm for a complex boundary without range point connections," IEEE Trans. Geosci. Remote Sens.,

vol.48, no.4, pp.1993–2004, April 2010.
[31] M. Noto S. Fang, S. Kidera, and T. Kirimoto, "Super-resolution time of arrival estimation using random resampling in compressed sensing," IEICE Trans. Commun., vol.E101-B, no.6, pp.1513–1520, June 2018.
[32] V.U. Zavorotny and A.G. Voronovich, "Comparison of geometric optics and diffraction effects in radar scattering from steep and breaking waves," Proc. IEEE International Geoscience and Remote Sensing Symposium, July 2007.
[33] T. Ohmori, S. Takahashi, and S. Kidera, "Gaussian mixture model parameter optimization in range points migration-based three-dimensional radar imaging," IEEE Sensors J., vol.21, no.12, pp.13594–13602, June 2021.
[34] S. Kidera, Y. Sasaki, S. Fang, T. Kirimoto, K. Saho, and T. Sato, "Three-dimensional imaging method incorporating range points migration and Doppler velocity estimation for UWB millimeter-wave radar," IEEE Geosci. Remote Sens. Lett., vol.14, no.1, pp.122–126, Jan. 2017.
[35] Federal Communications Commission, "Part 15 of the Commission Rs Rules Regarding Ultra-Wideband Transmission Systems," Subpart F, FCC–USA.
[36] H.P. Kriegel, M. Schubert, and A. Zimek, "Angle-based outlier detection in high-dimensional data," Proc. KDD, 2008.
[37] Y. Akiyama, T. Ohmori, and S. Kidera, "*k*-space decomposition-based 3-D imaging with range points migration for millimeter-wave radar," IEEE Trans. Geosci. Remote Sens., vol.59, no.8, pp.6637–6650, 2021.

Takumi Hayashi received the B.E. degree in electrical and electronic engineering from the University of Electro-Communications, Tokyo, Japan, in 2018, and the M.E. degree in informatics and communication engineering from the University of Electro-Communications, Tokyo, Japan, in 2020.

Takeru Ando received the B.E. degree in communication engineering and informatics from the University of Electro-Communications, Tokyo, Japan, in 2020. He is currently pursuing the M.E. degree with the Graduate School of Informatics and Engineering in the University of Electro-Communications, Tokyo, Japan. His research interest includes signal processing and imaging for millimeter wave radar as well as its applications.

Shouhei Kidera his B.E. degree in Electrical and Electronic Engineering from Kyoto University in 2003 and M.I. and Ph.D. degrees in Informatics from Kyoto University, Kyoto, Japan, in 2005 and 2007, respectively. He has been with Graduate School of Informatics and Engineering, the University of Electro-Communications, Tokyo, Japan, since 2009, and is currently an Associate Professor. His current research interest is in advanced radar signal processing or electromagnetic inverse scattering issue for ultra wideband (UWB) three-dimensional sensor or bio-medical applications. He has been stayed at the Cross-Disciplinary Electromagnetics Laboratory in the University of Wisconsin Madison as the visiting researcher in 2016. He has been a Principal Investigator of the PRESTO Program of Japan Science and Technology Agency (JST) from 2017 to 2021. He was a recipient of the 2012 Ando Incentive Prize for the Study of Electronics, 2013 Young Scientist's Prize by the Japanese Minister of Education, Culture, Sports, Science and Technology (MEXT), and 2014 Funai Achievement Award. He is a senior member of the Institute of Electrical and Electronics Engineering (IEEE), and a member of the Institute of Electrical Engineering of Japan (IEEJ), and the Japan Society of Applied Physics (JSAP).